A Novel Thermal Network Model Used for Temperature Calculation and Analysis on Brushless Doubly-Fed Generator With Winding Encapsulating Structure

Xiaodong Jiang, *Student Member, IEEE*, Yue Zhang, *Student Member, IEEE*, Shi Jin, *Member, IEEE*, Fengge Zhang, *Member*, *IEEE*, and Chris Gerada, *Senior Member, IEEE*

Abstract—In recent years, magnetic-barrier rotor has been put forward for brushless doubly-fed generator (BDFG) application owing to its desirable performance, such as high power density and strong magnetic coupling ability. However, it also causes significant losses induced by harmonics and high temperature problem. Hence, it is a major challenge to evaluate BDFG temperature rise fast and accurately. So far, aiming at magnetic-barrier rotor, there has no accurate thermal network model established achieving this goal. In addition, wingding end encapsulating technology has been used for a few years and its heat dissipation potential is determined by the materials. Therefore, the application of novel material in winding encapsulating structure is desirable to improve the heat dissipation potential. In this paper, an equivalent thermal network model, thermal resistance models of magnetic-barrier rotor and winding encapsulating structure with novel materials are further established for thermal analysis. Subsequently, temperature distributions for BDFG components are also calculated by finite element method (FEM), while the results are compared with those by analytical method. The BDFG prototype is manufactured with experimental tests performed. The correctness of the equivalent thermal network models proposed in this paper is verified by the test results.

Index Terms—Brushless doubly-fed generator (BDFG), equivalent thermal network model, magnetic-barrier rotor, temperature rise, winding encapsulating technology.

X. Jiang, S. Jin and F. Zhang are with Shenyang University of Technology, Shenyang, 110870, China (e-mail: jiangxd1207@163.com; wby-js@163.com; zhangfg@sut.edu.cn;).

Y. Zhang is with the School of Electronics, Electrical Engineering and Computer Science, Queens University Belfast, Belfast BT9 5AH, U.K (e-mail: yzhang35@qub.ac.uk).

Chris Gerada is with the Power Electronics, Machines and Control Group, University of Nottingham, Nottingham NG7 2RD, U.K (e-mail: chris.gerada@nottingham.ac.uk).

I. INTRODUCTION

IN recent years, brushless doubly-fed generators (BDFG) have attracted extensive attention for wind power generation system due to their attractive characteristics such as high reliability, low operating and maintenance cost, small capacity converter and power factor adjustable[1]-[4].

However, rich harmonics can be found in the magnetic field of BDFG. It is induced by the BDFG structure, as two sets of windings (power winding and control winding) accommodated in the same stator, magnetic field modulation effect by rotor structure[5]-[8]. Therefore copper losses and iron core losses of BDFGs are relatively larger than conventional electrical machines, which lead to high temperature issues in brushless doubly-fed machine[9]. Excessive high operational temperature of BDFG accelerates the aging effect and threatens the performance of generator insulation materials. Therefore, it is necessary to calculate BDFG temperature rise fast and accurately and restrict it by the application of effective cooling for BDFG.

At present, the methods of electrical machine thermal calculation mainly include simplified formula method, numerical computation method and thermal network method [10]. The simplified formula method is a relatively simple method, but it needs a lot of simplified treatments, which results in rough calculation and large error. Numerical computation method mainly includes finite element method and finite volume method. However the two methods mentioned above not only require higher grid precision, but also take more calculation time. It is notable that thermal network method effectively overcomes the disadvantages of the above methods and has widely used in the thermal calculation of permanent magnet motors [11], [12] and induction motors [13], [14]. However it has rarely been used for BDFG so far due to its complicated rotor structure which makes the heat transfer relation between nodes more complex.

In addition, one conventional cooling way for electrical machines is installing a fan at motor end, which excites the air flowing through the surface of motor frame to limit motor temperature rise [15]-[17]. Another way can be adopted for motor is water cooling. Its cooling effect is found better than

fan cooling [18]-[22]. For the cooling ways introduced above, they both need auxiliary devices such as fan and water pump, which lead to a reduction in motor efficiency. Therefore, seeking another way of cooling which not only improves the efficiency but also enhances the heat dissipation potential is of great significance.

In order to solve the problems mentioned above, in this paper, a novel equivalent thermal network model of BDFG, thermal resistance calculation models of magnetic-barrier rotor and winding encapsulating structure adopting new mixed materials used for enhancing heat dissipation potential are proposed for the thermal calculation for the first time.

This paper is organized as follows. In Section II, the winding, magnetic-barrier rotor and operating principles for BDFG are introduced. Then, the winding end encapsulating technology is described in Section III. As following, the equivalent thermal network model of BDFG and thermal resistance models of magnetic-barrier rotor and winding end encapsulating structure are proposed and established to predict BDFG temperature analytically in Section IV. In Section V, The BDFG temperature is also estimated by FEM, while the results are further compared with those obtained by analytical method. Finally, temperature experiment test is performed on a prototype and the correctness of the equivalent thermal network model proposed in this paper is validated.

II. STRUCTURE AND OPERATING PRINCIPLE

A. Winding Structure and Basic Parameters

The structure of BDFG is similar as induction machine. The only difference is the special magnetic-barrier rotor and windings in stator slot. In detail, the power winding is placed close to the slot opening, while the control winding is located at the slot bottom. The power and control winding are both connected by Y connection with the application of distributed, short-pitch winding type. The stator winding topology structure and wiring diagram are presented in Fig.1. Moreover, the fan is selected for cooling system. The basic parameters of BDFG are given in Table I.

(a)

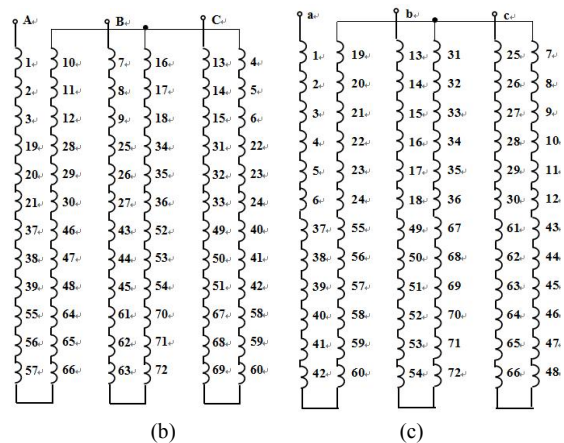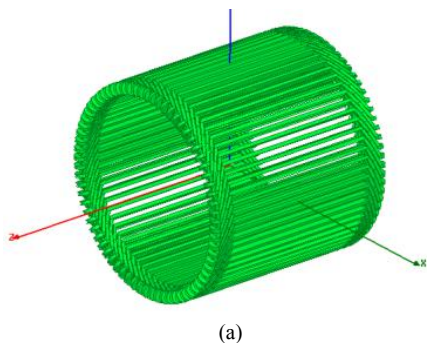(b)   (c)

Fig. 1 Winding topology structure and wiring diagram (a) winding topology structure (b) power winding wiring diagram (c) control winding wiring diagram

TABLE I
THE BASIC PARAMETERS OF BDFG

Item	Value
Rated power	11kW
Operating speed	500r/min
Stator outer diameter	400mm
Stator inner diameter	285mm
Rotor outer diameter	284mm
Slot number	72
Core length	225mm
Rated voltage	380V
Power winding rated current	17A
Control winding rated current	25A
The number of pole-pairs of power winding	4
The number of pole-pairs of control winding	2
Insulation class	F
Slot insulation material	DMD insulation paper
Insulation thickness	0.15mm
Mass flow rate	4900m^3/h
Wind pressure	100Pa

B. A Novel Magnetic-barrier Rotor

The magnetic field modulation capability between BDFG winding is realized by special rotor structure. Normally, there are two main topology structures for BDFG rotor, namely cage rotor and reluctance rotor. Special concentric short-circuit cage bar is utilized by cage rotor, with the advantage of simple processing craft accompanied. Whereas, its coupling capacity is worse, which reduces generator power density and induces significant copper losses. For reluctance rotor coupling capacity differs with structures. For example, the coupling capacity of ordinary salient pole reluctance rotors are weaker than magnetic-barrier reluctance rotors; the coupling capacity of axial laminated (ALA) reluctance rotors are more stronger, whereas, its axial overall tile structure may induces eddy current and impacts generator efficiency. Reference[23] proposes a radial laminated magnetic-barrier rotor structure, which reduces eddy current loss effectively and improves performance. In this paper, a novel magnetic-barrier rotor structure (the material is silicon steel sheet, DW310) is shown in Fig.2, which overcomes the above problems dramatically. Compared with similar rotor structure used in synchronous machines of reluctance, the magnetic-barrier rotor in BDFG plays a different role on magnetic field modulation mechanism

which is to realize the indirect coupling of power winding and control winding. The introduced rotor structure contains four magnetic layers and three magnetic-barrier layers (air layers). Moreover, connecting ribs are placed between each of two magnetic layers for playing a fixed role. The size and number of magnetic layers can determine the magnetic field modulation effect of BDFG. Compared with other rotor structures used in BDFG, the magnetic-barrier rotor can not only enhance the magnetic field modulation capability significantly but also further improve the power density and efficiency.
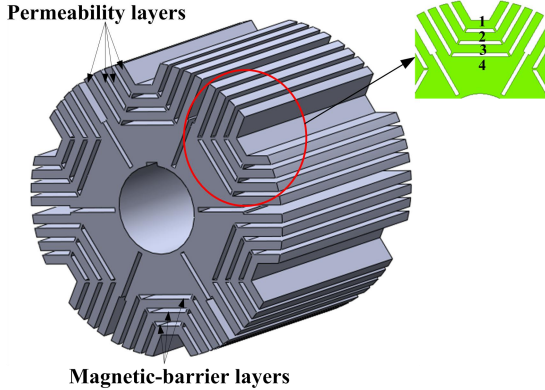

Fig. 2 A Novel magnetic-barrier rotor

C.   Operating Principle

The stator slots have two sets of windings with different pole numbers. The power winding is directly connected to the grid and the control winding is fed through the converter. The operation principle diagram is given in Fig.3.
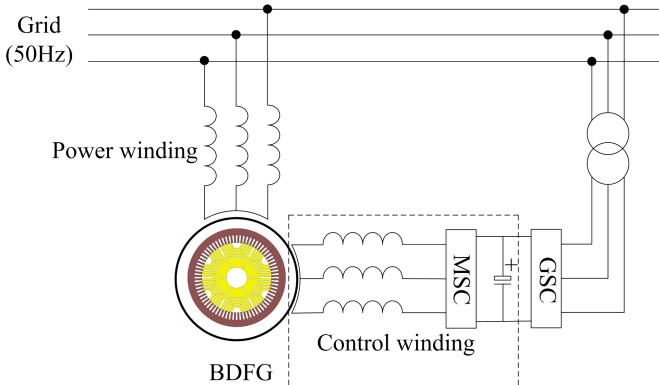

Fig. 3. The operating principle of BDFG

The relationship between frequency, pole pairs and operating speed of the BDFG is as [24]:

$$f_p = \frac{n_r \left(p_p + p_c \right)}{60} \pm f_c \qquad (1)$$

where f_p is the supplied line frequency (also known as the frequency of power winding); n_r is the rotor speed in rpm; p_p and p_c are the pole pair of the power and control windings, respectively; f_c is the converter frequency (also known as the frequency of control winding).

III.   WINDING END ENCAPSULATION TECHNOLOGY

A.   Description

Generally, the winding ends are located outside the stator slots and the thermal exchanging between them is mainly performed by the convection with air surrounded. However, it is well known that heat transfer by convection between solid and fluid is far less effective than that between solid and solid in electrical machine. The encapsulation technology of winding end using the above principle has been proposed to improve the heat dissipation capacity of electrical machines[25], [26]. However, the ability of taking away heat mainly depends on encapsulation structural materials. In this paper, a new kind of mixed materials which form the pouring mixture is proposed and used in the wingding encapsulation structure.

B.   Pouring mixture

The pouring mixture is made up by ethoxyline resin with grinding beaumontage added. This specific material does not contain solvents and halogens, with the characteristics of smaller heat release and lower shrinkage in the curing process. It has desirable electrical and mechanical properties with effective heat dissipation capability after curing. The main physical properties of pouring mixture after curing are listed in Table II.

TABLE II
THE MAIN PHYSICAL PROPERTIES OF POURING MIXTURE

Item	Value
Surface condition	Brightness
Density (25ºC)	1.61-1.62 g/cm^3
Hardness (SHORE D/15)	85-90
Pyroconductivity	0.85-0.95 W/(m·K)
Dielectric constant (25ºC)	4.0-5.0
Shrink factor (25ºC)	30-50×10^{-3}
Dielectric strength (25ºC)	21-24 kVm^{-2}
The highest running temperature after curing	155 ºC

C.   Using Craft

1) Pretreatment

It is necessary to check whether the resin has padding sediment during processing. If there is, the resin needs to be mixed well. A moderate amount of curing agent should be added to the resin and careful stirring is demanded to avoid air entry. The winding ends encapsulated needs to be preheated and the air in the mixed resin needs to be drawn out.

2) Encapsulating Craft

The craft requires to be encapsulated artificially in a vacuum and cured at room temperature.

3) Curing Craft

The pouring mixture can be solidified at room temperature and also continue to be heating after curing at room temperature to obtain a better resin stability, which assist to achieve optimum insulation performance.

D.   Storing

Epoxy resin and curing agent are required to be stored in a sealed container with a dry and cool circumstance. For the expired resin or storing under abnormal conditions, the padding

can be precipitated. Therefore, it is necessary to mechanically stirred before utilization. In addition, long-term storage can also lead to padding sediment, hence, it requires stirring before utilization.

IV. TEMPERATURE CALCULATION AND ANALYSIS BASED ON EQUIVALENT THERMAL NETWORK MODEL

A. Equivalent Thermal Network Model

In order to study the heat transfer principles between regions of BDFG, the equivalent thermal network model is established. Each part of BDFG is divided into orthogonal griddings according to the heat dissipation characteristics. Subsequently the orthogonal griddings are connected between each other via conduction and convection thermal resistances. The temperature results for each nodes are solved with the developed MATLAB program.

According to the principle of equivalent thermal network method, the whole structure of BDFG is divided into network nodes as displayed in Fig.4.
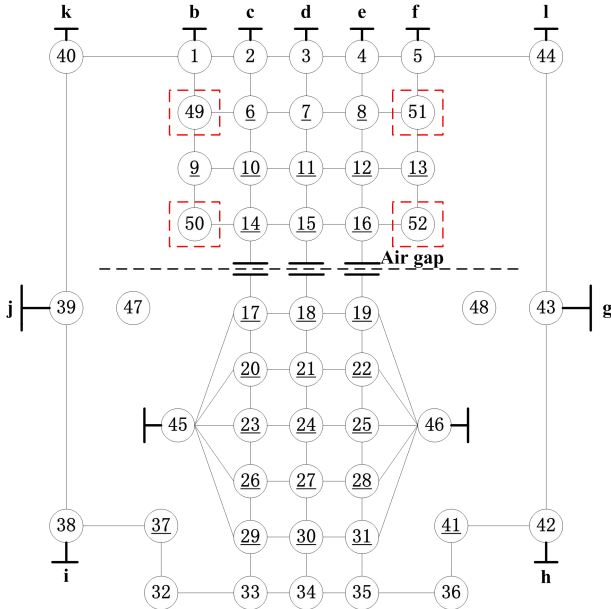

Fig. 4. Equivalent thermal network node distribution map

In Fig.4, 1~5 represent the frame nodes; 6~8 represent stator yoke nodes; 9~13 represent winding nodes, especially 9 and 13 are respectively end winding nodes; 14~16 represent stator tooth nodes; 17~31 are rotor part nodes. In detail, 17~19 are the first magnetic layer nodes; 20~22 are the second magnetic layer nodes; 23~25 are the third magnetic layer nodes; 26~28 are the fourth magnetic layer nodes and 29~31 are the fifth magnetic layer nodes. 32~36 represent shaft nodes; 37 and 41 respectively represent front and rear bearing nodes; 38~40 represent front end cover nodes and 42~44 represent rear end cover nodes; 45 and 46 respectively represent front and rear rotor pressure plate nodes; 47 and 48 respectively represent front and rear air nodes; 49~52 are the pouring mixture nodes; b~l are the outer air nodes.

In addition, the stator yoke and tooth iron core losses are distributed in 6~8 nodes and 14~16 nodes equably; the winding copper losses are equably distributed in 9~13 nodes and the mechanical losses are equably distributed in 37 and 41 node.

As the thermal resistance models for frame, stator tooth and yoke, shaft, end cover and winding of BDFG are identical with conventional induction motor, hence, this paper only presents the thermal resistance models for pouring mixture and novel magnetic-barrier rotor.

B. Thermal Resistance Model of Pouring Mixture

There are three basic heat transfer modes respectively including thermal conduction, convection and radiation. Because the temperature of electrical machine is relatively lower, thermal radiation is not considered under normal circumstance.

The conduction thermal resistance can be expressed as:

$$R_d = \frac{L_i}{S_d \lambda} \tag{2}$$

The convective thermal resistance is calculated as below:

$$R_d = \frac{1}{\alpha_v S_v} \tag{3}$$

where L_i is heat transfer distance; α_v is the convection heat transfer coefficient, S_d is the heat conduction area; S_v is the convection heat transfer area and λ is the heat conductivity coefficient.

1) The thermal resistance between pouring mixture and frame

There are three paths between pouring mixture and frame for heat transfer. One is internal heat conduction within the frame, one is internal heat conduction within the pouring mixture, last path is the mounting clearance between them.

The thermal resistance between node 49 and node 1 can be expressed as:

$$R_{fr-pm} = \frac{h_c}{2\lambda_{pm} S_{pm-ra}} + \frac{th_{fr}}{2\lambda_{fr} S_{fr-ra}} + \frac{L_{fr-pm}}{\lambda_{air} S_{fr-ra}} \tag{4}$$

$$S_{pm} = \pi D_1 oLfr_1 \tag{5}$$

$$S_{fr} = \pi\left(D_1 - \frac{h_c}{2}\right)oLfr_1 \tag{6}$$

where h_c is the stator core yoke thickness; th_{fr} is the frame thickness; L_{fr-pm} is the mounting clearance between frame and pouring mixture; λ_{pm}, λ_{fr} and λ_{air} are respectively the heat conductivity coefficient of pouring mixture, frame and air. S_{pm-ra}, S_{fr-ra} are the radial heat conductivity area, respectively; D_1, $oLfr_1$ are respectively the stator outer diameter and pouring mixture axial length.

2)The thermal resistance between pouring mixture and stator yoke

Three paths are connecting pouring mixture and stator yoke for heat transfer. One is internal heat conduction within pouring

mixture, one is internal heat conduction within stator yoke, while the third path is the mounting clearance between them.

The thermal resistance between node 49 and node 6 can be written as:

$$R_{pm\text{-}sy} = \frac{L_{fr} - L}{4\lambda_{pm}S_{pmy}} + \frac{L}{6\lambda_{si}S_{sy}} + \frac{L_{pm\text{-}sy}}{\lambda_{air}S_{sy}} \tag{7}$$

$$S_{pmy} = S_{sy} = \frac{\pi\left[D_1^2 - (D_1 - 2h_c)^2\right]}{4} \tag{8}$$

where L_{fr}, L and $L_{pm\text{-}sy}$ are respectively frame axial length, stator axial length and mounting clearance between pouring mixture and stator yoke; λ_{si} is the heat conductivity coefficient of silicon steel sheet. S_{pmy} and S_{sy} respectively represent the axial heat conductivity area of pouring mixture and stator yoke.

3)The thermal resistance between pouring mixture and stator tooth

There are also three paths connecting pouring mixture and stator tooth for heat transfer. One is internal heat conduction within pouring mixture, one is internal heat conduction within stator tooth, and the third path is the mounting clearance between them.

The thermal resistance between node 50 and node 14 can be expressed as:

$$R_{pm\text{-}st} = \frac{L_{fr} - L}{4\lambda_{pm}S_{pmt}} + \frac{L}{6\lambda_{si}S_{st}} + \frac{L_{pm\text{-}st}}{\lambda_{air}S_{st}} \tag{9}$$

$$S_{pmt} = S_{st} = b_{t1}Z_1 h_s \tag{10}$$

where $L_{pm\text{-}st}$ is mounting clearance between pouring mixture and stator tooth; S_{pmt} and S_{st} respectively represent the axial heat conductivity area of pouring mixture and stator tooth.

4) The thermal resistance between pouring mixture and winding end

Winding ends are encapsulated by pouring mixture. The pouring mixture structure approximates as stator core structure, which also consists of "pouring mixture yoke" and "pouring mixture tooth". The thermal resistance between node 49, 50 and node 9 can be both written as:

$$R_{pmy\text{-}wi} = \frac{\delta_i}{\lambda_{pm}} + \frac{1}{4}\left[\frac{b\left(1 - \sqrt{S_f}\right)}{\lambda_L}K_L + \frac{b\left(1 - \sqrt{S_f}\right)}{\lambda_{air}}\cdot\left(1 - K_L\right)\right.$$
$$\left. + \frac{d - d_w}{\lambda_d}\frac{b\sqrt{S_f}}{d}\right] \tag{11}$$

$$b = 2R_s - \frac{1}{3}\left(2R_s - b_{s1}\right) \tag{12}$$

where b is the "pouring mixture slot" width; S_f is the "pouring mixture slot" copper space factor; δ_i is the equivalent slot insulation thickness; d, d_w are respectively enameled wire outside diameter and bare wire diameter. λ_L, λ_d are respectively the heat conductivity coefficient of dipping varnish and wire lacquer layer. K_L is the insulation paint filling factor. R_s and b_{s1} are the slot size parameters.

The thermal resistance models of node 51 and 52 can refer to node 49 and 50 due to the symmetrical structure.

C.   *Thermal Resistance Model of Magnetic-Barrier Rotor*

The magnetic-barrier rotor is relatively complicated; hence, it needs to be simplified by ignoring the narrow connected ribs between magnetic layers in building thermal resistance model.

The thermal resistance between node 17 and node 14 can be expressed as:

$$R_{1417} = \frac{1}{\alpha_g S_{1417}} \tag{13}$$

where α_g is the air gap heat dissipation coefficient and S_{1417} is the heat radiating area. Besides,

$$\alpha_g = \frac{N_u \lambda}{g} \tag{14}$$

$$S_{1417} = \frac{(2e_1 + 2H_{11} + Q_{11})L}{3} \tag{15}$$

where N_u is the air gap Nusselt coefficient; g is the air gap length; e_1 is each magnetic layer width; The magnetic layer parameters are shown in Fig.5; In Fig.5, the subscripts i equals to 1,2,3,4 and denotes different magnetic layer parameters, respectively.
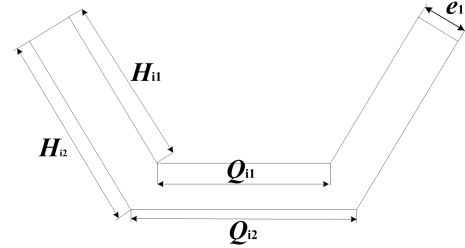

Fig. 5. Rotor magnetic layer structure

The thermal resistance between node 17 and 18 can be calculated as:

$$R_{1718} = \frac{L}{3p\lambda_{si}S_{1718}} \tag{16}$$

where p is the rotor equivalent number of pole-pairs and S_{1718} is the axial heat conductivity area. Besides,

$$S_{1718} = (H_{11} + H_{12})e_1 + \frac{(Q_{11} + Q_{12})e_1}{2} \tag{17}$$

The heat conduction paths between node 17 and 20 include the heat conduction within the first magnetic layer, the convective heat dissipation of the first air layer and the heat conduction within the second magnetic layer, which are denoted by R_{17201}, R_{17202} and R_{17203}, respectively.

$$R_{17201} = \frac{e_1}{2S_{17201}\lambda_{si}} \tag{18}$$

where S_{17201} is the radial heat conductivity area. Besides,

$$S_{17201} = \frac{p \cdot (2H_{12} + Q_{12}) \cdot L}{3} \qquad (19)$$

$$R_{17202} = \frac{1}{S_{17201}\alpha_r} \qquad (20)$$

where α_r is the rotor end face heat dissipation coefficient. Besides,

$$\alpha_r = \frac{2N_{ur}\lambda_{air}}{D_2} \qquad (21)$$

$$N_{ur} = 1.67 R_{er}^{0.385} \qquad (22)$$

$$R_{er} = \frac{\pi n D_2^2}{120\gamma} \qquad (23)$$

where N_{ur} is the rotor end face air Nusselt coefficient, R_{er} is the air Reynolds number; D_2 is rotor outer diameter; γ is the aerodynamic viscosity coefficient and n is the rotate speed.

$$R_{17203} = \frac{e_1}{2S_{17202}\lambda_{si}} \qquad (24)$$

where S_{17202} is the radial heat conductivity area. Besides,

$$S_{17202} = \frac{(2H_{21} + Q_{21})pL}{3} \qquad (25)$$

Therefore, thermal resistances between node 17 and node 20 can be written as:

$$R_{1720} = R_{17201} + R_{17202} + R_{17203} \qquad (26)$$

The thermal resistance between node 17 and node 45 can be expressed as:

$$R_{1745} = \frac{L}{6p\lambda_{si}S_{1718}} + \frac{L_{ro\text{-}pl}}{p\lambda_{air}S_{1718}} + \frac{h_g}{2p\lambda_{ec}S_{1718}} \qquad (27)$$

where $L_{ro\text{-}pl}$ is the mounting clearance between rotor and baffle; h_g is the end cover thickness; λ_{ec} is the heat conductivity coefficient of end cover.

In a similar way, the thermal resistance models of node 18~25 may refer to that of node 17.

Since there is no air gap between the fourth and fifth magnetic layers, hence, the heat exchange modes between them are different from the first three magnetic layers. The structural diagram and relevant parameters are presented in Fig.6.
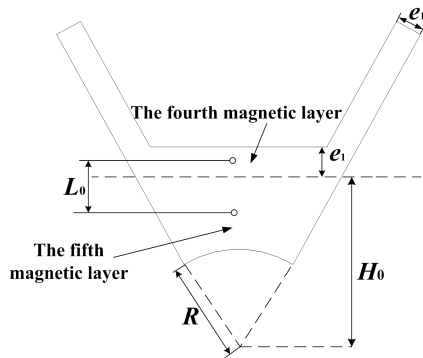

Fig. 6. The fourth and fifth magnetic layer structure

The node 26 exchanges heat with stator tooth node 14, axial layer node 27, the third magnetic layer node 23, the fifth magnetic layer node 29, rotor front pressure plate node 45 and air, respectively. Among them, the thermal resistance modes between node 26 and 14, 27, 23,45 may refer to node 17 and the thermal resistance between node 26 and 29, margin air just be given as follow.

The thermal resistance between node 26 and 29 can be expressed as:

$$R_{2629} = \frac{L_0}{p\lambda_{si}S_{2629}} \qquad (28)$$

where L_0 is the distance between center nodes of the fourth and fifth magnetic layers and S_{2629} is the radial heat conductivity area. Besides,

$$S_{2629} = \frac{pQ_{42}L}{3} \qquad (29)$$

The thermal resistance between node 26 and margin air can be written as:

$$R_{26air} = \frac{1}{S_{26air}\alpha_r} \qquad (30)$$

where S_{26air} is the heat radiating area. Besides,

$$S_{26air} = \frac{2pH_{42}L}{3} \qquad (31)$$

In a similar way, the thermal resistance models of node 27 and 28 may refer to node 26.

The node 29 exchanges heat with axial layer node 30, the fourth magnetic layer node 26, rotor front pressure plate node 45, shaft node 33 and air, respectively. Among them, the thermal resistance modes between node 29 and 45 are the same between node 17 and 45. This paper just gives the thermal resistances between node 29 and 30, node 29 and 33.

The thermal resistance between node 29 and 30 can be written as:

$$B_{2930} = \frac{L}{3\lambda_{si}S_{2930}} \qquad (32)$$

where S_{2930} is the axial heat conduction area. Besides,

$$S_{2930} = \left(\frac{Q_{42}H_0}{2} - \pi\frac{R^2}{6}\right)p \qquad (33)$$

The thermal resistance between node 29 and 33 can be written as:

$$R_{2933} = \frac{L_{mc}}{\lambda_{air}S_{2933}} \qquad (34)$$

where L_{mc} is the assembly clearance. S_{2933} is the axial heat conduction area. Besides,

$$S_{2933} = \frac{\pi D_{i2} L}{3} \qquad (35)$$

where D_{i2} is the rotor inner diameter.

In addition, The thermal resistance between node 29 and margin air can be expressed as:

$$R_{29air} = \frac{1}{\alpha_r S_{29air}} \qquad (36)$$

where S_{29air} is the heat radiating area. Besides,

$$S_{29air} = \left[\frac{H_0}{\cos(\pi/6)} - R \right] \frac{2L}{3} p \qquad (37)$$

In a similar way, the thermal resistance models of node 30 and 31 may refer to that of node 29.

D. Heat Conductivity Coefficient

The heat conductivity coefficients are closely related to the materials. The materials of various parts of BDFG can refer to those of conventional induction motor. The heat conductivity coefficients are listed in Table III and the unit is W/m·K.

TABLE III
THE MAIN HEAT CONDUCTIVITY COEFFICIENTS

Parts	X direction	Y direction	Z direction
Stator/Rotor core	39	39	4.43
Power and control winding	385	385	385
Insulation	0.26	0.26	0.26
Frame/End cover	39.2	39.2	39.2
Bearing/Shaft	50.2	50.2	50.2
Pouring mixture	0.95	0.95	0.95
Air	0.0305	0.0305	0.0305

E. Heat Conductance Equation

As mentioned previously, the heat transfer principles between the internal nodes of magnetic-barrier rotor BDFG have been analyzed. For the NTH node, the heat balance equation is usually expressed as:

$$-G(1,n)T_1 - G(2,n)T_2 - \cdots - G(n-1,n)T_{n-1} + G(n,n)T_n \\ - G(n+1,n)T_{n+1} - \cdots - G(52,n)T_{52} = W_n \qquad (38)$$

where $G(n,n)$ is the NTH node self-heat conductance and $G(i,n)$ ($i=1,2,..n-1,n+1,...52$) is the NTH node mutual heat conductance.

The heat balance equations of 52 nodes are simultaneous and can be written as:

$$GT = W \qquad (39)$$

where G is the heat conductivity matrix; T is each node temperature and W is the thermal sources.

F. Losses Calculation

Due to the special magnetic-barrier rotor structure which influences the magnetic field modulation effect, the harmonic magnetic fields in BDFG are quite abundant. The power losses of BDFG, which acting as thermal sources, requires to be estimated for the generator thermal analysis. The main losses of BDFG can be concluded as copper loss and iron loss, and they are introduced in the following.

The copper losses of winding can be obtained by:

$$P_{cuw} = 3I_p^2 R_p + 3I_c^2 R_c \qquad (40)$$

where I and R respectively represent the phase current and resistance. The subscripts p and c denote the power winding and control winding, respectively.

Compared with copper loss, BDFG iron core loss estimation is more complicated. Conventional iron loss analysis method adopts constant hysteresis and eddy-current loss coefficients for iron core estimation[27], which may induce large computational error. Therefore, this paper uses the iron loss calculation model of [28] [29], since it includes variable loss coefficients for more precision. The iron loss model can be formulated as follows:

$$W_{ie} = \frac{D}{2\pi^2} \int_{iron} \frac{1}{N} \sum_{k=1}^{N} \left\{ K_{er}(f,B_r) \left(\frac{B_r^{k+1} - B_r^k}{\Delta t} \right)^2 + K_{e\theta}(f,B_\theta) \left(\frac{B_\theta^{k+1} - B_\theta^k}{\Delta t} \right)^2 \right\} dv \qquad (41)$$

$$W_{ih} = \frac{D}{2T} \sum_{i=1}^{NE} \frac{\Delta V_i}{2} \left(\sum_{j=1}^{N_{pr}^i} K_{hr}(f,B_{mr}^{ij})(B_{mr}^{ij})^2 + \sum_{j=1}^{N_{p\theta}^i} K_{h\theta}(f,B_{m\theta}^{ij})(B_{m\theta}^{ij})^2 \right) \Delta V_i \qquad (42)$$

where ΔV_i is the volume of each mesh element. f is the dominant frequency of each flux density waveform. Δt is the sampling time and T is the sampling period. B_{mr} and $B_{m\theta}$ are the magnitudes of the rotational and tangential flux densities, respectively.

FEM is utilized to verify the correctness of the calculation model of iron loss and copper loss. The results are shown in Fig.7.
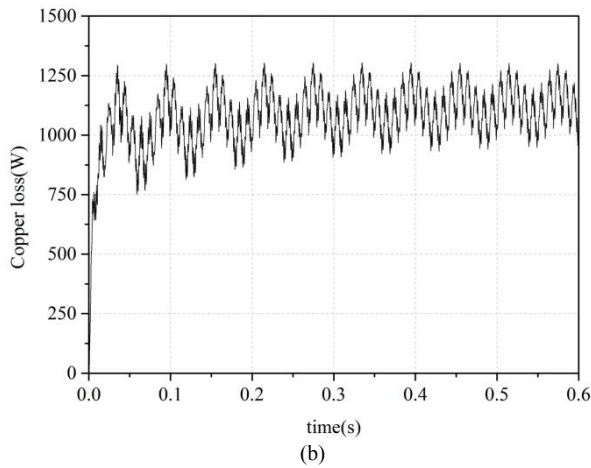

(a)

(b)
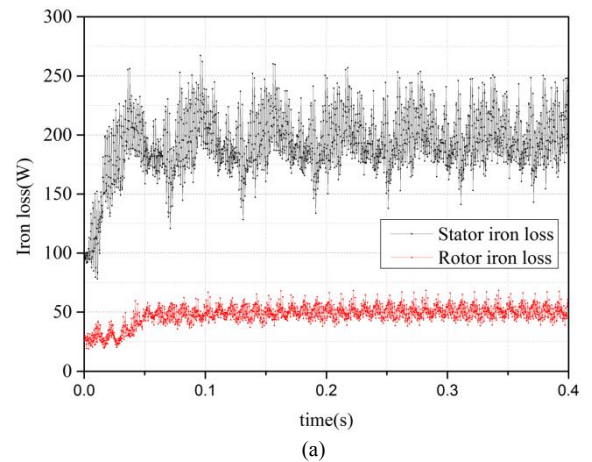
Fig.7 FEM calculation results (a) iron core loss (b) copper loss

Fig.8 shows the loss calculation comparison results obtained by analytic method and FEA. It can be found that the loss results calculated by analytic method nearly agree with those obtained by FEM. In addition, according to the design and processing experience, the mechanical loss is selected approximately 2% of the rated power in this paper.
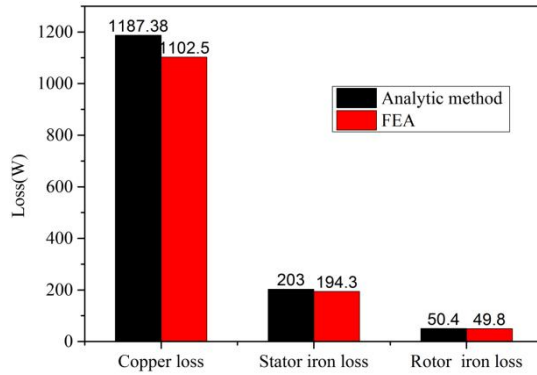

Fig.8 Loss calculation comparison results

The temperature results of BDFG all nodes obtained by the thermal network method are calculated by MATLAB program, with the results listing in Table IV.

TABLE IV
THE TEMPERATURE RESULTS OF EACH NODE

Items	Node temperature/ºC				
Frame	(1)43.88	(2)68.65	(3)70.87	(4)68.64	(5)43.84
Stator yoke	(6)74.63	(7)75.97	(8)74.62		
Wingding	(9)86.86	(10)83.62	(11)83.53	(12)83.61	(13)86.84
Stator tooth	(14)81.10	(15)81.56	(16)81.10		
First magnetic layer	(17)82.59	(18)83.76	(19)82.59		
Second magnetic layer	(20)83.41	(21)85.55	(22)83.4		
Third magnetic layer	(23)81.54	(24)82.81	(25)81.53		
Fourth magnetic layer	(26)77.42	(27)75.61	(28)77.41		
Fifth magnetic layer	(29)77.74	(30)75.52	(31)77.72		
Shaft	(32)73.92	(33)77.63	(34)75.54	(35)77.61	(36)73.91
Bearing	(37)72.97				(41)72.95
Front end cover	(38)71.85	(39)16.78	(40)35.08		
Rear end cover	(42)71.84	(43)16.04	(44)34.86		
Rotor pressure plate	(45)68.35		(46)68.36		
Inner cavity air	(47)66.45		(48)66.43		
Pouring mixture	(49)77.73	(50)86.85	(51)77.71	(52)86.84	

V. TEMPERATURE SIMULATION CALCULATION

FEM is also utilized for temperature estimation for the BDFG with magnetic-barrier rotor. Fig.9 and Fig.10 present the temperature calculation results for the magnetic-barrier rotor and the stator iron core, respectively. In Fig.9, the rotor highest temperature is found as 84.03ºC, which occurs at the rotor ends. In Fig.10, the highest temperature of stator core reaches up to 84.13ºC and the hottest position locates at stator tooth. In addition, the temperature decreases along the radial direction gradually.
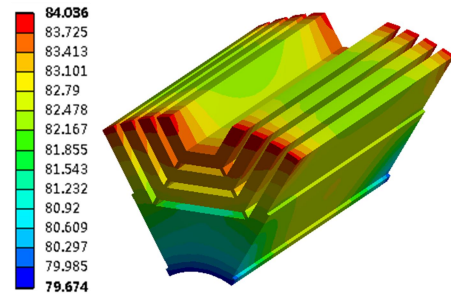

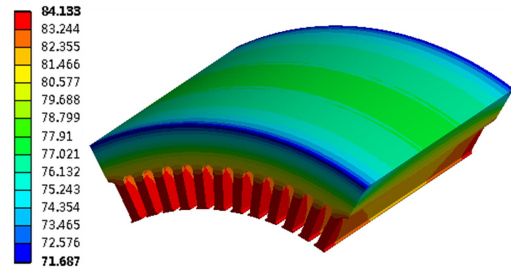Fig. 9. Rotor temperature distribution

Fig. 10. Stator core temperature distribution

Fig.11 displays the pouring mixture temperature estimation result. Due to the presence of pouring mixture, which increases the heat conduction area of winding end with stator core and frame, the temperature gradient is conspicuous. It is noticeable that the temperature of the area contacting with stator core ranging from 75.08ºC to 86ºC along the radial direction, while the temperature variation tendency is gradually reducing along the axial direction with the temperature ranging from 64.16ºC to 75.08ºC.
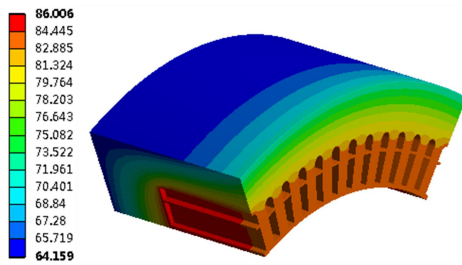
Fig. 11. Pouring mixture temperature distribution

Table V provides the comparison between temperature estimation results by FEM. Situation I represents adopting winding end encapsulating technology and Situation II is not using this technology.

TABLE V
THE COMPARISON BETWEEN TEMPERATURE SIMULATION RESULTS

Item	Temperature/ºC	
	Situation I	Situation II
Stator core	71.69~84.13	79.08~93.25
Rotor core	79.67~84.04	87.31~93.1
Power winding	82.03~85.91	90.65~95.7
Control winding	81.82~85.91	90.42~95.72
Shaft	69.31~82.65	74.34~90.98
Frame	61.84~77.17	68.58~85.67
Bearing	68.32~71.55	73.11~77.13

It can be observed from Table V that the temperatures of BDFG components adopting winding end encapsulating technology are lower than their counterparts without winding end encapsulating adopted.

In addition, the comparison between temperature results calculated by equivalent thermal network method and FEM respectively are also shown in Table VI.

TABLE VI
THE COMPARISON BETWEEN TEMPERATURE RESULTS CALCULATED BY TWO DIFFERENT METHODS

Item	Temperature/ºC	
	Equivalent thermal network	FEM
Stator core	74.62~81.56	71.69~84.13
Rotor core	75.52~85.55	79.67~84.04
Power winding	83.53~86.86	82.03~85.91
Control winding	83.53~86.86	81.82~85.91
Shaft	73.91~77.63	69.31~82.65
Frame	43.84~70.87	63.84~77.17
Bearing	72.95~72.97	68.32~71.55

In Table VI, it can be seen that the temperature ranges of each part of BDFG calculated by the two methods are basically unanimous.

VI. EXPERIMENTAL VERIFICATION

In order to validate the correctness of the thermal network model proposed in this paper for magnetic-barrier rotor BDFG with winding encapsulating structure, the temperature test under synchronous power generation operation mode is performed. The experimental facilities of BDFG are mainly composed of BDFG prototype, frequency control induction motor (prime motor), frequency converter, AC intelligent dummy loads and temperature controller. In addition, the thermal resistances of type PT100 are embedded in the end and

middle position of power winding and control winding, respectively, and are also placed on the frame and stator tooth. The temperature values are observed by the temperature controller. The rotor pack and frame are given in Fig.12.
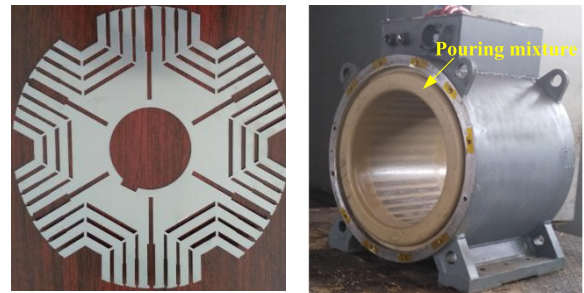

Fig. 12. (a)A magnetic-barrier rotor pack   (b) The frame structure

The temperature test curves of power and control winding end and middle, frame and stator tooth are shown in Fig.13. It is seen that the temperature values of test points mentioned above gradually become steady after 80 minutes. The stable temperature of the end of power winding and control winding are respectively 88.5ºC and 88.9ºC. The temperature values of power and control winding in stator slot are correspondingly 85.7ºC and 85.9ºC. In addition, the temperature values of stator tooth and frame are stable at 84.4ºC and 59.2ºC. Temperature results obtained from equivalent thermal network, FEM and experiment are displayed in Fig.14. From Fig.14, it can be observed that the temperature values of the end and middle position of power winding, control winding and stator tooth obtained from two estimation methods are both approaching to the test results. In addition, since the test point on the frame is actually located between node 1 and 2, so the frame temperature result calculated by thermal network method is approximately selected the average temperature of two nodes here, which makes the error of frame temperature bigger comparing with test result.
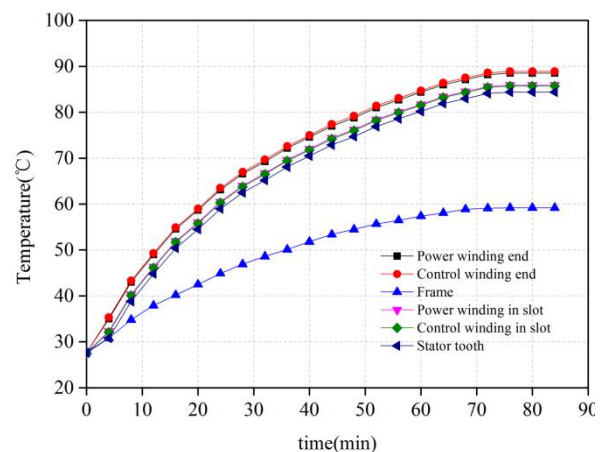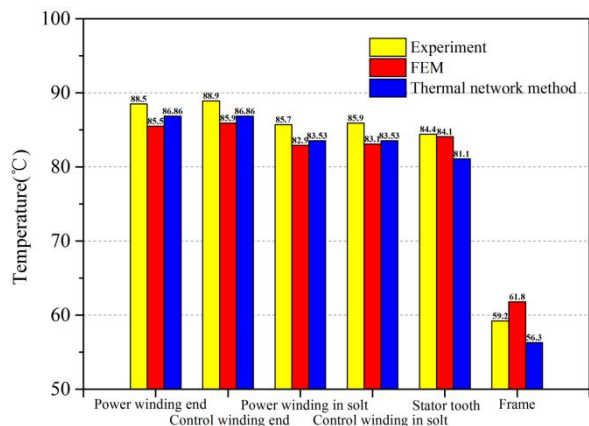

Fig. 13. Temperature test curves

Fig. 14. The comparison of temperature results obtained by three methods

VII. CONCLUSION

This paper proposes a novel equivalent thermal network model, thermal resistance models of magnetic-barrier rotor and winding end encapsulating structure with novel mixed materials. It improves machine heat dissipation potential to analyze the heat transfer rules between internal structure parts and calculate the temperature rise of key positions of BDFG for the first time. The effectiveness of mixed materials used in the winding end encapsulating structure to enhance the heat dissipation ability for magnetic-barrier rotor BDFG is verified by comparing with the FEM results. Moreover, through the comparison between temperature results obtained by thermal network method, FEM and experimental test performed on BDFG prototype respectively, the correctness of proposed thermal network model are verified.

REFERENCES

[1] T. Long, S. Y. Shao, P. Malliband, E. Abdi, and R. A. McMahon, "Crowbarless fault ride through of the brushless doubly fed induction generator in a wind turbine under summetrical voltage dips", *IEEE Trans. Ind, Electron.*, vol. 60, no.2, pp. 2833-2841, Jul. 2013.

[2] S. Ademi, M. G. Jovanovic, and M. Hasan, "Control of brushless doubly-fed reductance generators for wind energy conversion systems", *IEEE Trans. Energy Conv.*, vol. 30, no.2, pp. 596-604, Jun. 2015.

[3] F. G. Zhang, S. Y. Yu, X. P. Wang, H. Wang, and S. Jin, "Research of a novel brushless doubly-fed generator with hybrid rotor", *IEEE Trans. Appl. Supercond.*, vol. 26, no.7, Art. no. 0608205, Oct. 2016.

[4] A. M. Knight, R. E. Betz, and D. G. Dorrell, "Design and analysis of brushless doubly fed reluctance machines", *IEEE Trans. Ind. Appl.*, vol. 49, no. 1, pp. 50-58, Jan. 2013.

[5] M.-F. Hsieh, I.-H. Lin, and D. Dorrell, "Magnetic circuit modeling of brushless doubly-fed machines with induction and reluctance rotors", *IEEE Trans. Magn.*, vol. 49, no. 5, pp. 2359-2362, May. 2013.

[6] X. Chen, Z. Wei, X. Cao, and C. Ye, X. Wang, "Research of voltage amplitude fluctuation and compensation for wound rotor brushless doubly-fed machine", *IEEE Trans. Energy Convers.*, vol. 30, no. 3, pp. 908-917, Sep. 2015.

[7] S. Y. Yu, F. G. Zhang, and H. Wang, "Parameter calculation and analysis of a novel wind power generator", *IEEE Trans. Magn.*, vol. 53, no. 11, Art. no. 8205607, Nov. 2017.

[8] H. Gorginpour, H. Oraee, and E. Abdi, "Calculation of core and stray load losses in brushless doubly fed induction generators", *IEEE Trans. Ind, Electron.*, vol. 61, no. 7, pp. 3167-3177, Jul. 2014.

[9] X. D. Jiang, F. G. Zhang, and X. L. Xu, "Temperature field calculation and experimental research on brushless doubly fed machine with hybrid rotor", in *Proc. ITEC Asia-Pacific*, Harbin, China 2017, pp. 1-6.

[10] A. Boglietti, A. Cavagnino, D. Staton, M. Shanel, M. Mueller, and C. Mejuto, "Evolution and modern approaches for thermal analysis of

electrical machines", *IEEE Trans. Ind, Electron.*, vol. 56, no. 3, pp. 871-882, Mar. 2009.

[11] M. Polikarpova, P. Ponomarev, P. Roytta, S. Semken, Y. Alexandrova, and J. Pyrhonen, "Direct liquid cooling for an outer-rotor direct-drive permanent-magnet synchronous generator for wind farm applications", *IET Electr. Power Appl.*, vol. 9, no. 8, pp. 523-532, Mar. 2015.

[12] D. G. Dorrell, "Combined thermal and electromagnetic analysis of permanent-magnet and induction machines to aid calculation", *IEEE Trans. Ind, Electron.*, vol. 55, no. 10, pp. 3566-3574, Jul. 2008.

[13] A. Boglietti, A. Cavagnino, M. Popescu, and D. Staton, "Thermal model and analysis of wound-rotor induction machine", *IEEE Trans. Ind. Appl.*, vol. 49, no. 5, pp. 2078-2085, Sep/Oct. 2013.

[14] S. Mezani, N. Takorabet, and B. Laporte, "A combined electromagnetic and thermal analysis of induction motors", *IEEE Trans. Magn.*, vol. 41, no. 5, pp. 1572-1575, May. 2005.

[15] S. Mizuno, S. Noda, M. Matsushita, T. Koyama, and S. Shirishi, "Development of a totally enclosed fan-cooled traction motor", *IEEE Trans. Ind. Appl.*, vol. 49, no. 4, pp. 1508-1514, Jul/Aug. 2013.

[16] T. Nakahama, K. Suzuki, S. Hashidume, F. Ishibashi, and M. Hirata, "Cooling airflow in unidirectional ventilated open-type motor for electric vehicles", *IEEE Trans. Energy Convers.*, vol. 21, no. 3, pp. 645-651, Sep. 2006.

[17] A. Boglietti, A. Cavagnino, D. Staton, M. Shanel, M. Mueller, and C. Mejuto, "Evolution and modern approaches for thermal analysis of electrical machines", *IEEE Trans. Ind. Electron.*, vol. 56, no. 3, pp. 871-882, Mar. 2009.

[18] C. Jungreuthmayer, T. Bäuml, O. Winter, M. Ganchev, H. Kapeller, A. Haumer, and C. Kral, "A detail heat and fluid flow analysis of an internal permanent magnet synchronous machine by means of computational fluid dynamics", *IEEE Trans. Ind. Electron.*, vol. 59, no. 12, pp. 4568-4578, Dec. 2012.

[19] G. Zhang, W. Hua, M. Cheng, B. F. Zhang, and X. B. Guo, "Coupled magnetic-thermal fields analysis of water cooling flux-switching permanent magnet motors by an axially segmented model", *IEEE Trans. Magn.*, vol. 53, no. 6, Art. no. 8106504, Jun. 2017.

[20] P. Zheng, R. R. Liu, P. Thelin, E. Nordlund, and C. Sadarangani, "Research on the cooling system of a 4QT prototype machine used for HEV", *IEEE Trans. Energy Convers.*, vol. 23, no. 1, pp. 61-67, Mar. 2008.

[21] A. Fasquelle and D. Laloy, "Water cold plates cooling in a permanent magnet synchronous motor", *IEEE Trans. Ind. Appl.*, vol. 53, no. 5, pp. 4406-4413, Sep/Oct. 2017.

[22] M. Satrústegui and M. Martinez-Iturralde, J. C. Ramos, P. Gonzalez, G. Astarbe, I. Elosegui, "Design criteria for water cooled systems of induction machines", *Applied Thermal Engineering*, vol. 114, pp. 1018-1028, Mar. 2017.

[23] Xu L Y, Guan B, and Liu H J, "Design and control of a high-efficiency doubly-fed brushless machine for wind power generator application", in *Proc. IEEE ECCE*, Atlanta, USA 2010, pp. 1-7.

[24] X. D. Jiang, F. G. Zhang, and Y. G. Li, "The research on temperature field and flow field of brushless doubly-fed generator with cage-barrier rotor", in *Proc. IEEE ISIE*, Edinburgh, UK, 2017, pp. 381-386.

[25] E. Fairall, C. Rheberhegen, E. Rowan, J. Lo, B. Bilgin, and A. Emadi, "Maximizing thermal effectiveness and minimizing parasitic loss in a liquid cooled switched reluctance machine", in *Proc. IEEE ITEC*, Dearborn, MI, USA 2016, pp. 2409-2416.

[26] H. D. Li, K. W. Klontz, V. E. Ferrell, and D. Barber, "Thermal models and electrical machine performance improvement using encapsulation material", *IEEE Trans. Ind. Appl.*, vol. 53, no. 2, pp. 1063-1069, Mar/Apr. 2017.

[27] K. Yamazaki, "Torque and efficiency calculation of an interior permanent magnet motor considering harmonic iron losses of both the stator and rotor", *IEEE Trans. Magn.*, vol. 39, no. 3, pp. 1460-1463, May. 2003.

[28] X. K. Sun and M. Cheng "Thermal analysis and cooling system design of dual mechanical port machine for wind power application", *IEEE Trans. Ind. Electron.*, vol. 60, no. 5, pp. 1724-1733, May. 2013.

[29] J. H. Seo, S.-Y. Kwak, S.-Y. Jung, C.-G. Lee, T.-K. Chung, and H.-K. Jung, "A rersearch on iron loss of IPMSM with a fractional number of slot per pole", *IEEE Trans. Magn.*, vol. 45, no. 3, pp. 1824-1827, Feb. 2009.

Xiaodong Jiang (S'18) was born in Shenyang, China. He received the B.E., and M.S., degrees from Shenyang University of Technology, Shenyang, China, in 2011 and 2014, respectively, both in electrical engineering. He is currently working toward the PH.D. degree in Electrical Engineering at Shenyang University of Technology, China. His current research interests mainly include the design of permanent magnet motor and brushless doubly-fed machine, special motor thermal calculation and wind power generation.

Yue Zhang (S'15) was born in Shenyang, China. He received the B.Eng. degree from Shenyang University of Technology, Shenyang, China, in 2011, the M.Eng. degree from Zhejiang University, Hangzhou, China in 2014, and the Ph.D. degree in Queen's University Belfast, Belfast, U.K., in 2018. His research interests include the design and analysis of electrical machines for industrial applications and electrical vehicles.

Shi Jin (M'17)was born in 1981. She received the B.E., M.S., and Ph.D. degrees from Shenyang University of Technology, Shenyang, China, in 2004, 2007, and 2011, respectively, all in electrical engineering.

Her research interests mainly include power electronic technology, electrical machines and their control systems, and wind power generation. For the last several years, she has undertaken two research projects supported by the National Natural Science Foundation of China. She has authored or coauthored 54 papers published in important academic journals and presented at domestic and international conferences, of which 44 were cited by SCI/EI.

Fengge Zhang (M'17) was born in 1963. He received the B.E., M.S., and Ph.D.degrees from the Shenyang University of Technology, Shenyang, China, in 1984,1990, and 2000, respectively, all in electrical engineering. From 2001 to 2005, he was a Senior VisitingScholar and Visiting Professor at Esslingen University of Applied Sciences, Esslingen, Germany. For the last several years, he has been authorized 15National Invention Patents and published more than 200 papers in important academic journals and international conference proceedings on electrical machines and control systems, of which 120 were cited by SCI/EI.

Chris Gerada (M'05) received the Ph.D. degree in numerical modeling of electrical machines, in 2005, from The University of Nottingham, Nottingham, U.K., where he was also a Researcher of high performance electrical drives and the design and modeling of electromagnetic actuators for aerospace applications. Since 2006, he has been the Project Manager of the GE Aviation Strategic Partnership. In 2008, he was a Lecture in electrical machines, in 2011, was an Associate Professor, and in 2013, was a Professor in The University of Nottingham. His main research interests include the design and modeling of high-performance electric drives and machines. He is currently an Associate Editor for the IEEE TRANSACTIONS ON INDUSTRY APPLICATIONS and the Past Chair of the IEEE IES Electrical Machines Committee.